Nanotoxicology, June 2011; 5(2): 140–156

informa
healthcare

Dispersion stabilization of silver nanoparticles in synthetic lung fluid studied under *in situ* conditions

ROBERT I. MACCUSPIE, ANDREW J. ALLEN, & VINCENT A. HACKLEY

Materials Science and Engineering Laboratory, National Institute of Standards and Technology (NIST), Gaithersburg, Maryland, USA

(Received 23 February 2010; accepted 26 May 2010)

Abstract
The dispersion stabilization of silver nanoparticles (AgNPs) in synthetic lung fluid was studied to interrogate the effects on colloidal stability due to the principal constituents of the fluid. The colloidal stability of 20 nm citrate-AgNPs dispersed in the presence of each constituent of the synthetic lung fluid (individually, the complete fluid, and without additives) was observed during titration of increasing sodium chloride concentration. A variety of complementary *in situ* measurement techniques were utilized, including dynamic light scattering, ultraviolet-visible absorption spectroscopy, atomic force microscopy, and small-angle X-ray scattering, which provided a collective set of information that enabled far better understanding of the dispersion behavior in the fluid than any one technique alone. It was observed that AgNPs continued to adsorb bovine serum albumin (BSA) protein from the synthetic lung fluid solution as the sodium chloride concentration increased, until a maximum BSA coating was achieved prior to reaching the physiological sodium chloride concentration of 154 mmol L^{-1}. BSA was determined to be the constituent of the synthetic lung fluid that is required to provide colloidal stability at high salt loadings, though the phospholipid constituent exerts a subtle effect. Additionally, as AgNPs are a distinctly different class of nanoparticles apart from the carbon nanotubes and titanium dioxide nanoparticles initially reported to be dispersible using this fluid, this work also demonstrates the broad applicability of synthetic lung fluid in providing stable dispersions for engineered nanoparticles for use in biological assays.

Keywords: *AgNPs, synthetic alveolar lavage fluid, nanoparticle dispersion protocol, nanoEHS, SAXS flow cell*

Introduction

Silver nanoparticles (AgNPs) have recently emerged as the most commonly identified nanoscale material in consumer products (Maynard 2009). Although nanoscale silver has applications ranging from conductive inks used for printing circuit components (Perelaer et al. 2009) to its use as an imaging contrast agent (Koh et al. 2008) and in surface plasmon resonance (SPR)-based bioaffinity sensing (Aslan et al. 2004, 2005), its principal use in consumer products is based on its broad-spectrum biocidal properties (Raffi et al. 2008; Gardner and Jones 2009). The antimicrobial effect is well documented for the soluble ionic form of silver, which has been used as a treatment for drinking water supplies from antiquity to modern day space flight (Tien et al. 2008). It remains unclear if nanoscale silver presents a new form of silver or is simply a new vector for solubilized silver ions (Luoma 2008). Consequently, research on the environmental, health, and safety (EHS) impact and risk of AgNPs has gained substantial momentum in the past few years (Wijnhoven et al. 2009), and public awareness has clearly increased in tandem (Henig 2007). There is a growing body of published work on the toxicity of AgNPs ranging from inhalation studies (Hussain and Schlager 2009) to species-specific models (Kim et al. 2009; Kvitek et al. 2009; Yeo and Yoon 2009) to reactive oxygen species generation and DNA damage (Ahamed et al. 2008; Rahman et al. 2009).

However, one of the common challenges facing nanoEHS and toxicology researchers is achieving reproducible AgNP dispersions in order to control and quantify the delivered dose in an *in vitro* or *in vivo* experimental scenario (Wiesner et al. 2009). While a variety of approaches to synthesize AgNPs have been reported in the literature (Naik et al. 2002; Yu et al.

Correspondence: Dr Robert I. MacCuspie, National Institute of Standards and Technology, Ceramics Division, 100 Bureau Dr, MS 8520, Gaithersburg, MD 20899-8520, USA. Tel: +1 301 975 6064. Fax: +1 301 975 5334. E-mail: robert.maccuspie@nist.gov

ISSN 1743-5390 print/ISSN 1743-5404 online © 2011 Informa UK, Ltd.
DOI: 10.3109/17435390.2010.504311

2003; Kramer et al. 2004; Muniz et al. 2005; Tomczak et al. 2007, 2008; Nam et al. 2008) since the first account of silver colloids by Carey Lea in 1889 (Carey Lea 1889), quantifying colloidal stability under biologically or environmentally relevant conditions is typically beyond the scope of these studies. Similarly, stability (or dispersability) has generally not been addressed in studies aimed at assessing the toxicity of AgNPs (Wijnhoven et al. 2009), although it is now widely recognized to be a critically important issue for the design and interpretation of such studies (Porter et al. 2008). For example, it has been reported that noble metal nanoparticles, like gold and silver, stabilized by only weakly bound ligands such as citrate will dynamically absorb and desorb proteins stochastically as the biological matrix they are exposed to changes (Cedervall et al. 2007; Lynch et al. 2007; Lundqvist et al. 2008). Formation of a protein corona is known to affect the physical properties (Nuraje et al. 2006; Voevodin et al. 2007; MacCuspie et al. 2008b, 2010a), by increasing the hydrodynamic size and also by providing increased colloidal stability from steric repulsion of the large proteinaceous shell (MacCuspie 2010b). However, rigorous physical characterization of the mechanisms of colloidal stabilization, in an EHS context, has not been widely reported (Skebo et al. 2007; Kvitek et al. 2009).

To provide a greater degree of reproducibility (and to mitigate salt-induced aggregation) in nanoparticle dispersion preparations while closely mimicking biological conditions, protocols using either alveolar lavage fluid (Sager et al. 2007) or synthetic mimics of alveolar lavage fluid (Porter et al. 2008) have recently been reported. Subsequent studies have cited the National Institute for Occupational Safety and Health (NIOSH) dispersion protocol (Porter et al. 2008) as a method of dispersing nanoparticles for toxicological studies (Sager et al. 2008; Erdely et al. 2009; Herzog et al. 2009a, 2009b; Sager and Castranova 2009; Shvedova et al. 2009). The key elements of that protocol involve using series-specific serum albumin protein at 0.6 mg mL^{-1} and 1,2-dipalmitoyl-*sn*-glycero-3-phosphocholine (DPPC) at 0.01 mg mL^{-1} in phosphate-buffered saline (PBS) to create a solution into which the desired nanoparticles are introduced. To probe the detailed behavior of AgNPs in this dispersion protocol, four main dispersions were explored: native citrate-AgNPs, bovine serum albumin (BSA) containing AgNPs, (BSA AgNPs), DPPC containing AgNPs (DPPC AgNPs), and BSA plus DPPC containing AgNPs (BSA + DPPC AgNPs). This series of samples probed the effect of each component separately, compared the described dispersion protocol as a positive control, and compared the native citrate-AgNP as a negative control. Within the context of this paper, the dispersions will also be referred to as coatings for the AgNPs, reflecting both the protocol's procedure to incubate the AgNPs with the synthetic lung fluid before final use and the assumption that BSA and DPPC molecules adsorb onto the surface of the AgNPs before the start of the titration experiments.

In situ techniques with temporal resolution of 1 min or less enabled us to study the dynamics of the colloidal suspensions, which otherwise were very challenging to obtain with such temporal fidelity by static and *ex situ* approaches. Specifically, calibrated small angle X-ray scattering (SAXS), provides the diameter of the core nanoparticle and can quantify population volume fractions *in situ* (Allen et al. 2008); SAXS is relatively insensitive to the presence of organic coronas. Furthermore, by combining the high brilliance of a synchrotron light source with flow-cell capabilities (Allen et al. 2008), real-time *in situ* measurements of aggregating nanoparticle dynamics can be achieved with time resolution of ≈1 min or better. By contrast, dynamic light scattering (DLS), a widely used measurement tool, provides the hydrodynamic envelope (spherical equivalent) diameter, including any associated soft material (corona), and is extremely sensitive to the presence of agglomerates. Finally, UV-vis spectrometry provides a measure of the concentration of metal nanoparticles based on their surface plasmon resonance (SPR) absorption signal, as the SPR of metal nanoparticles is well understood both theoretically (Link and El-Sayed 1999; Kelly et al. 2002; Duan et al. 2009) and experimentally (Elghanian et al. 1997; Malinsky et al. 2001; Frederix et al. 2003). Therefore, a simple colorimetric determination of the concentration of single AgNPs dispersed in a solution is possible by measuring the absorbance and using the Beer-Lambert law. Additionally, the characteristic AgNP SPR peak absorbance wavelength will slightly red-shift if coatings are present on the nanoparticle surface, or significantly red-shift if the particles aggregate (Malinsky et al. 2001; Kelly et al. 2002). To complement these *in situ* measurements, atomic force microscopy (AFM) and transmission electron microscopy (TEM) were employed as orthogonal techniques to assess nanoparticle size, and to visualize the degree and structure of aggregation when it occurred. The combination of these techniques provides a more complete picture than any single technique could provide by itself. For example, comparing DLS and SAXS results can allow estimation of the thickness of the corona of molecules sorbed onto the AgNP surface.

Titration across a range of saline concentrations, from hypotonic to isotonic to hypertonic, was utilized to interrogate the roles of electrostatic and steric

factors in the colloidal stabilization of each dispersion. Using the NIOSH protocol as a model, this work aims to provide fundamental knowledge for further refinement of dispersion protocols that either mimic true exposure conditions, or seek to best stabilize the nanoparticles under biologically or environmentally relevant conditions.

The selection of citrate-AgNPs as our model system was based on the consensus findings of a recent workshop jointly organized by the National Institute of Standards and Technology (NIST) and the US Army Corps of Engineers that addressed, in part, the selection of common test materials for cross-laboratory comparisons (Kennedy et al. 2009). Citrate stabilized AgNPs were nominated due their widespread use within the research community and because of the relative ease with which citrate can be displaced for other surface coatings (Wijnhoven et al. 2009). More complex nanomaterials (Matsui and MacCuspie 2001; Banerjee et al. 2004; Nuraje et al. 2004; MacCuspie et al. 2008a), including surface modified or coated materials used in commercial applications (Gao et al. 2005; Duan et al. 2009), were beyond the scope of this initial study.

Methods

Unless otherwise specified, all chemicals were purchased from Sigma Aldrich (St Louis, MO, USA)* of the highest quality available, and used as received without further purification. All solutions and suspensions were prepared using 18.2 MΩ Type I biological grade deionized water obtained from an Aqua Solutions (Jasper, GA, USA) water purification system. This paper will observe the following conventions when reporting data for the instrumental techniques selected: DLS data points are the mean of five measurements with uncertainties of one standard deviation; AFM images are representative of no less than 10 images collected per sample; the UV-vis data points are the mean of three measurements with uncertainties of one standard deviation; the SAXS data points are the mean calibrated intensities calculated from the data set at each Q value, with uncertainties of one standard deviation (SD).

AgNP synthesis

AgNPs were prepared by reduction of silver nitrate, similar to the Turkevich method for gold nanoparticles (Turkevich et al. 1951). For example, to 400 mL of boiling deionized water, 1.690 mL of 58.8 mmol L^{-1} aqueous silver nitrate and 2.920 mL of 34 mmol L^{-1} aqueous tribasic sodium citrate dehydrate were added while stirring at 600 rpm, before dropwise addition of 2.000 mL of 100 mmol L^{-1} aqueous sodium borohydride. The reaction was stirred for 30 min at a slow boil, then allowed to cool to room temperature on the hot plate. The cooled AgNP product solutions were purified by pressurized stirred cell ultrafiltration with 10,000 Da molecular weight cut-off regenerated cellulose filters, removing any unreacted reagents into the filtrate while the nanoparticles remained in the retentate. Ultrafiltration typically resulted in a concentration increase to approximately 0.4 mg of Ag mL^{-1}. Before experiments, the retained AgNP solutions were passed through a 0.2 μm polyvinylidene fluoride (PVDF) syringe filter to remove adventitious dust or large aggregates.

Dispersion preparation

Dispersions were prepared in a manner consistent with the NIOSH protocol (Sager et al. 2007; Porter et al. 2008). For the specific conditions used for each dispersion ligand combination refer to Supplementary Table SI-1, available online. Bovine serum albumin (BSA), Sigma number B4287, and 1,2-dipalmitoyl-*sn*-glycero-3-phosphocholine (DPPC), Sigma number P0763 were used as received. Briefly, stock AgNPs were added to the reaction vessel, followed by the ligand(s) of interest based on the dispersion. The dispersions were vortexed for 30 sec and allowed to stand for at least 24 h to ensure adequate equilibration before use in a titration. The NIOSH dispersion protocol specifies series-specific albumin. In this study, BSA was selected due to its widespread commercial availability, homology to human serum albumin, and less stringent biosafety requirements that allow a broader range of experimental techniques to be employed. The initial pH values of the citrate AgNPs, DPPC AgNPs, BSA AgNPs, and BSA + DPPC AgNPs were 7.42, 7.35, 7.48, and 8.01, respectively.

NaCl titrations

Titration experiments were performed by adding aliquots of 2.000 mol L^{-1} sodium chloride (NaCl) to the suspension of AgNPs. Details on the volumes for the *in situ* SAXS experiments can be found in Supplementary Table SI-2, available online. The SAXS reaction volumes were scaled down by a factor of 10 for UV-vis and DLS measurements, where the titration was performed in the cuvette by serial addition via micropipette in a HEPA-filtered particle-free

hood to prevent the introduction of dust particles. Separate solutions were prepared for the AFM measurements, with volumes scaled down by a factor of 100 compared to the SAXS reaction volumes, and only one aliquot of NaCl solution added to immediately advance to the desired titration step.

AFM and TEM instrumentation and methodology

AFM samples were prepared by incubating on poly-*L*-lysine coated mica substrates (see Supplementary material section, available online, for more details) using a protocol developed for imaging of NIST gold nanoparticle reference materials (2009). AFM measurements were performed using a Veeco Instruments (Santa Barbara, CA, USA) Dimension 3100 with a Nanoscope V controller operated in intermittent contact or tapping mode, using a closed-loop scanner. Cantilevers with nominal spring constants of 7.4 N m^{-1} (NanoAndMore, Lady's Island, SC, USA) were used to collect all images. TEM samples were prepared by dropcasting 4.0 μL of solution onto a Formvar-Carbon coated 200 mesh copper TEM grid (Ted Pella, Redding, CA, USA), and imaged on a JEOL Model JEM3010 TEM operating at 300 kV. A standard cross-grating was used to calibrate the magnification, and hence the scale bar for the TEM image.

UV-vis instrumentation and methodology

UV-vis spectra were collected on a Perkin Elmer (Waltham, MA, USA) Lambda 750 spectrophotometer in UV-transparent disposable plastic semimicrocuvettes (Brandtech, Inc., Essex, CT, USA) with a 1 cm path length, and requiring 1 mL sample volumes. AgNP solutions were diluted such that the initial absorbance was approximately 1. The spectrometer uses a split-beam configuration equipped with an 8 + 8 cell changer and water-jacketed temperature control. Equimolar NaCl solutions were used as reference and blank samples for each observed titration step. The effects on the wavelength of the SPR peak due to changes in the solvent's index of refraction as a result of the addition of NaCl were assumed to be negligible.

DLS instrumentation and methodology

DLS measurements were performed using a Malvern Instruments (Westborough, MA, USA) Zetasizer Nano in 173° backscatter. Sample preparation was performed in a particle-free hood. Disposable semimicro cuvettes were cleaned and dried immediately before use. Measurements were performed at (20.0 ± 0.1)°C. The viscosity and refractive index of the solvent were adjusted in the size calculation at each step of the titration to account for changing compositions. The cumulants analysis algorithm was applied to obtain the Z_{avg} equivalent hydrodynamic diameter and the polydispersity index (PI). The PI is a metric for the width of the size dispersion, and generally an increase in PI will be indicative of aggregation or other processes that introduce size heterogeneity. The DLS methodology followed recommendations outlined in the NIST-Nanotechnology Characterization Laboratory (NCL) protocol (2008) (Jillavenkatesa et al. 2001; NIST 2008a).

SAXS instrumentation and methodology

Pinhole SAXS measurements were carried out at beamline 15-ID-D (ChemMatCARS) of the Advanced Photon Source, Argonne National Laboratory, IL, USA. This instrument is described in detail elsewhere (Cookson et al. 2006). The AgNP suspensions are exposed to the X-ray beam by continuously flowing the sample in a closed loop from a polystyrene sample reservoir to a 1.4 mm quartz capillary positioned in the incident beam path. On average, the solution was cycled through the closed loop every 45 sec, or more than 30 cycles per titration step. Details of the custom-designed sample fluidics system are described elsewhere (Allen et al. 2008), and were modified here to handle smaller sample volumes as shown schematically in Figure 1. NaCl titrant was dispensed into the sample reservoir using a Hamilton (Reno, NV, USA) Microlab 500. Samples were irradiated with a (0.5 × 0.3) mm monochromatic X-ray beam (energy = 12 keV, λ = 0.103 nm), and experiments were performed at ambient temperature (about 20°C). The collected data were corrected for parasitic and solvent scattering, circularly averaged about the incident beam direction to yield 1-D SAXS data, and intensity-calibrated against a standard glassy carbon sample. To obtain quantitative nanoparticle volume fraction size distributions the calibrated 1-D SAXS intensity data, $I(Q)$ versus Q (where $Q = (4\pi/\lambda)\sin\Theta$ is the magnitude of the scattering vector, λ is the X-ray wavelength and Θ is half of the scattering angle), were analyzed using an entropy maximization algorithm known as MaxEnt (Potton et al. 1988). The SAXS data were reduced and analyzed (including implementation of MaxEnt) within the Irena 2 package of data evaluation and modeling macros for Igor Pro (Ilavsky and Jemian 2009). The reported volume

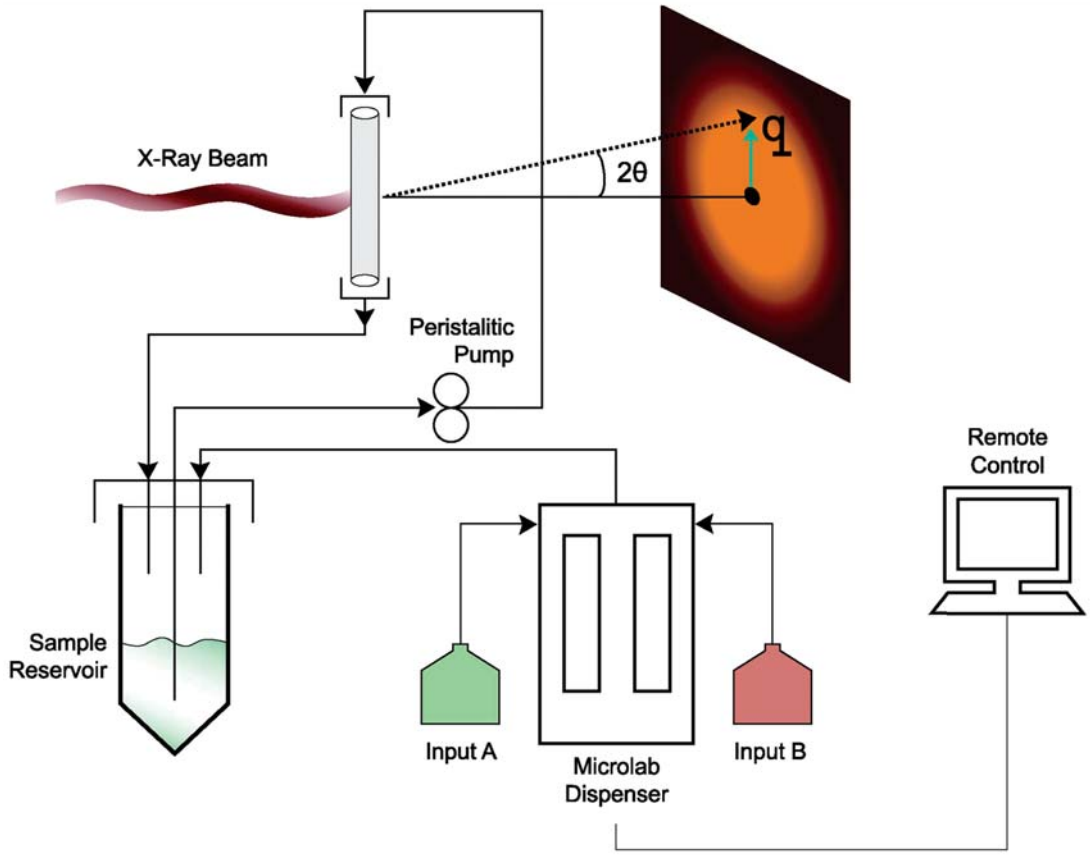

Figure 1. Schematic illustration of *in situ* SAXS capillary flow cell set up with remote controlled titration capability.

fractions were corrected for dilution by the NaCl titrant.

The program conditions used and further details in each titration experiment are detailed online in Supplementary Table SI-2, and further experimental details are provide in the online supplementary section. The suspensions were pumped at a rate of approximately 15 mL min^{-1}, with a closed loop volume of approximately 8 mL and the system containing between (10 and 12) mL of sample for each run. On average the solution was cycled through the system every 45 sec, or more than 30 cycles per titration step.

Results

DLS

DLS was employed during the course of titrations to monitor the hydrodynamic size of structures dispersed in solution, namely the average diameter (Z_{avg}) and polydispersity index (PI). Figure 2 shows a plot of the mean hydrodynamic diameter of the four AgNP dispersions through the course of the titration with NaCl. The citrate-AgNPs began to form larger structures at a NaCl concentration as low as 20 mmol L^{-1}. As the titration continued, the citrate-AgNPs quickly formed very large structures, with diameters exceeding 1 μm at 50 mmol L^{-1} NaCl. The DPPC AgNPs behaved similarly to the citrate-AgNPs, with an observable size increase after the first stepwise addition of NaCl to a concentration of 10 mmol L^{-1}. Also similar to the citrate-AgNPs, the DPPC AgNPs formed structures exceeding 1 μm in size at 50 mmol L^{-1} NaCl. For the DLS titrations, it was concluded the citrate-AgNPs and DPPC AgNPs were nearly completely aggregated at 50 mmol L^{-1} of NaCl, due to the observed size increase of nearly two orders of magnitude; thus, the titration was halted.

The BSA AgNPs, however, exhibited a more stabilized behavior. As the NaCl concentration approached 100 mmol L^{-1}, the observed diameter of the BSA AgNPs increased incrementally. Quantitatively, the mean Z_{avg} diameter went from 22.5 ± 0.6 nm in deionized water to 33.0 ± 0.8 nm at 100 mmol L^{-1}, an increase of ΔZ_{avg} = 10.5 ± 1.0 nm while the PI remained relatively constant (as

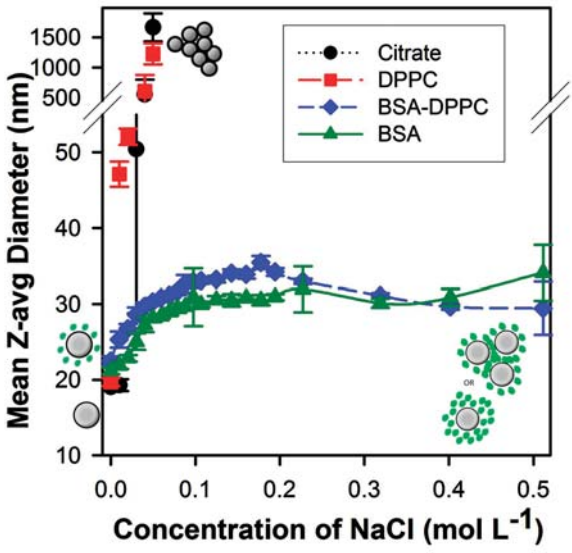

Figure 2. Mean Z_{avg} diameter by dynamic light scattering as a function of NaCl concentration for titration of citrate (black circles), DPPC (red squares), BSA (green triangles), BSA + DPPC (blue diamonds) AgNPs. Lines are guide to the eye. Uncertainty is one standard deviation.

shown in Supplementary Information Figure SI-1, available online). Above the 100 mmol L^{-1} NaCl concentration, there was no further increase in diameter observed. The BSA + DPPC AgNPs also exhibit a stabilized behavior, following a similar pattern to the BSA AgNPs, suggesting the increased colloidal stability at very high salt concentrations is derived primarily from the BSA as opposed to the DPPC.

It is worth noting that a subtle difference was observed with and without the DPPC present at NaCl concentrations between (100 and 200) mmol L^{-1}, where the mean Z_{avg} diameter transiently increased from 32.9 ± 0.8 nm at 97.6 mmol L^{-1} to a maximum of 35.4 ± 0.9 nm at 181 mmol L^{-1} in the case of BSA AgNPs. At higher NaCl concentrations, the mean Z_{avg} diameter decreased by 5.8 ± 1.0 nm to 29.6 ± 0.4 nm at 458 mmol L^{-1}, while the PI remained relatively constant. In contrast, the BSA+DPPC AgNPs appeared to reach a steady state above 100 mmol L^{-1} of NaCl with the mean Z_{avg} diameter not changing in a statistically significant fashion.

Microscopy

A representative TEM image of the initial AgNP products is shown in Figure 3. To investigate the aggregation states of the various AgNPs, AFM images were collected of each of the AgNP dispersions in deionized water and two representative NaCl concentrations from the titration, as shown in Figure 4. AgNPs were deposited in a manner that minimized the possibility of artifact agglomerate formation during deposition. While no less than ten images were analyzed per sample, only one representative image is displayed here for simplicity. The Figure is arranged in a three by four image fashion such that each row contains a different sample coating – from top to bottom citrate, DPPC, BSA, and BSA + DPPC – and each column contains a different NaCl concentration (from left to right) 0 mmol L^{-1}, 50 mmol L^{-1} and 160 mmol L^{-1}.

For both the citrate and the DPPC AgNP dispersions, a significant decrease in the number of single AgNPs per field of view was observed concurrently with the appearance of much larger structures. For the BSA containing AgNP dispersions, no decrease in the number of AgNPs per field of view was observed. Additionally, no aggregated structures were observed, as single nanoparticles were found to be the predominant structure.

UV-vis spectrometry

To assess the concentration of AgNPs that remained in solution over time, titration experiments were performed that mimicked the DLS titrations and UV-vis spectra were collected every 8 min (Figure 5) for 24 min at each concentration described in the first four columns of Supplementary Table SI-2, available online. In Figure 5a, the absorption at a wavelength of 395 nm is plotted as a function of the NaCl concentration. All data points in Figure 5(a) were normalized to account for changes in concentration due to the dilution effect of adding NaCl solution to the AgNP suspension. Each data point corresponds to a step in the titration, and is the mean of the three spectra collected during the 24 min immediately after addition of the salt. For AgNP dispersions in which BSA was absent, a decrease was observed in absorbance to nearly zero by the 50 mmol L^{-1} NaCl step. For AgNP dispersions with BSA present, the normalized absorbance remained fairly constant throughout the titration.

The full spectra collected at step 1 (10 mmol L^{-1}) and step 5 (50 mmol L^{-1}) are shown in Figures 5b and 5c, respectively. From the spectra at low salt concentration, it is clear that BSA caused a red-shift in the AgNP adsorption peak by approximately 10 nm. This red-shift was constant even at the highest NaCl concentrations studied. As NaCl is increased to 50 mmol L^{-1} as in step 5, the absorbance of single citrate-AgNPs decreases markedly, but the peak appears not to shift.

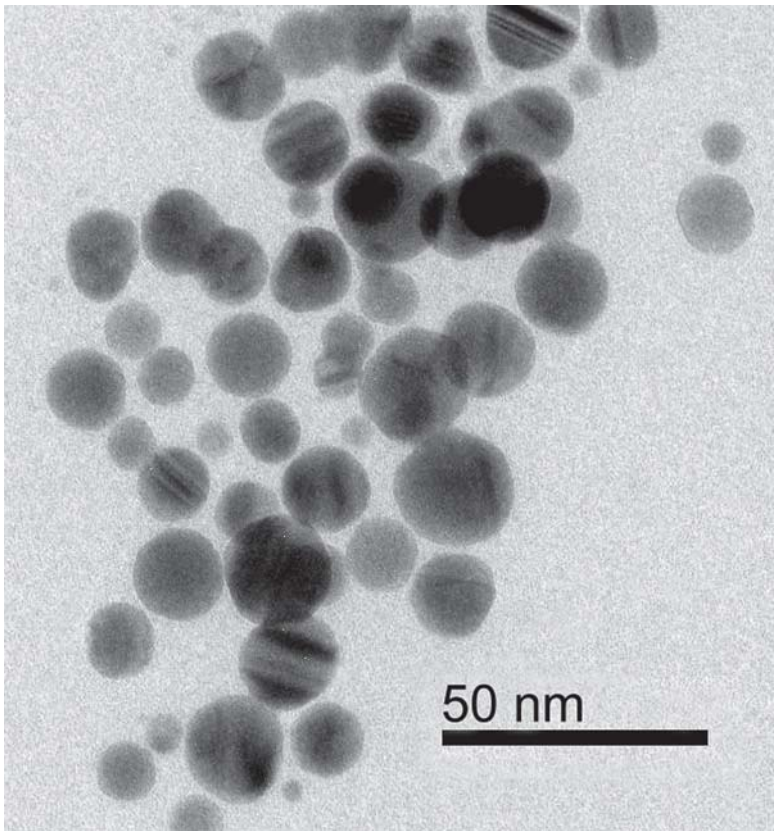

Figure 3. Representative TEM image of stock citrate AgNPs. Scale bar is 50 nm.

SAXS

Figure 6 shows a sampling of the reduced SAXS data for each titration, omitting most of the collected data sets for the sake of clarity. The relative scattering intensities are shown, measured with respect to the maximum intensity for the initial 'control' condition. From Figure 6a, the intensity of the scattering signal decreased throughout the first five steps of the titration by over an order of magnitude. A similar decrease is observed in Figure 6b from the DPPC AgNP dispersion. Additionally, the shape of the curves was evolving over time in both the citrate-AgNP and DPPC AgNP cases, suggesting changes to the characteristic dimensions and structure of the AgNPs. The broad knee in the control curve near $Q = 0.9\ \text{nm}^{-1}$ disappeared quite early in the titration, within the first few additions of NaCl. The main trend in the scattering profile appeared to be a shift towards lower Q (i.e., longer length scales), especially in the DPPC dispersion, although this could not be confirmed due to the Q limitations of the instrument configuration used in this study. In Figure 6c and 6d, the shape of the curves for the BSA AgNP and BSA + DPPC AgNP dispersions, respectively, was generally conserved throughout the course of the NaCl titration; moreover the intensity for the BSA AgNP and BSA + DPPC AgNP dispersions was essentially constant over much of the Q range for tens of hours after the start of the titration.

In Figure 7a, SAXS results for the total volume fraction of primary particles are reported as a function of the titration step, normalized against the fraction of the dwell time completed for each titration step. For example, a data point at normalized titration step 4.5 indicates that 50% of the dwell time for that step had elapsed since the addition at step 4. For visual clarity, only a representative sampling of the data was plotted. Figure 7a shows for reference a secondary x-axis on the top of the graph providing the approximate NaCl concentration corresponding to the titration steps. The volume fraction of single (unaggregated) citrate-AgNPs and single DPPC AgNPs in solution decreased rapidly during the first five titration steps, as shown in Figure 7a. The information afforded on these two dispersions by the temporal resolution of the SAXS measurements will be described in the subsequent discussion section. The normalized volume fraction of single AgNPs in the BSA and BSA + DPPC dispersions remained fairly constant, with a similar amount of fluctuation compared to the UV-vis data.

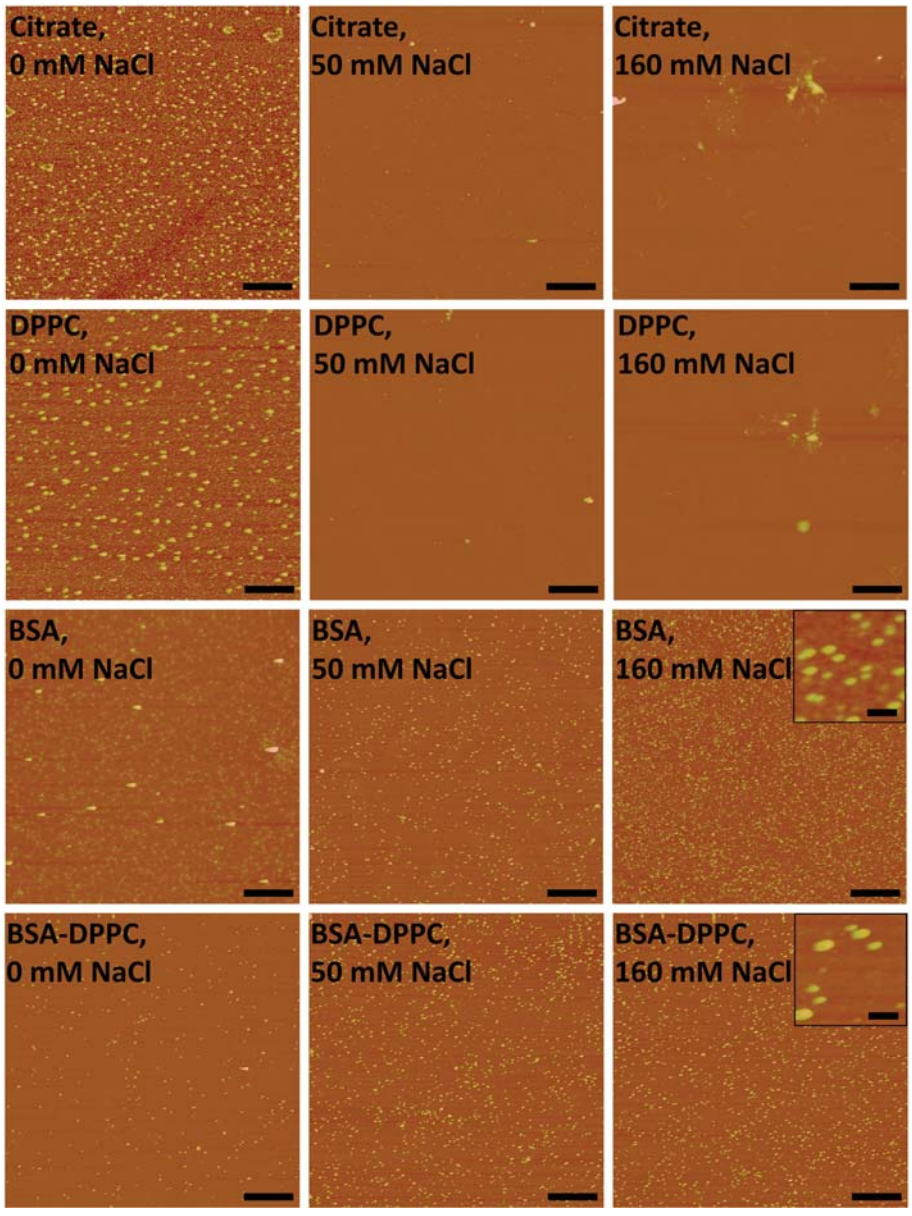

Figure 4. AFM height images of citrate (top row), DPPC (second row), BSA (third row), and BSA + DPPC (bottom row) AgNPs in deionized water (left column), 50 mmol L^{-1} (center column), and 160 mmol L^{-1} (right column) of NaCl. Insets are digital magnifications of 2048 × 2048 pixel images shown. Scale bars are 1 μm for images, and 100 nm for insets.

Figures 7b and 7c show absolute calibrated intensity data for two datasets taken from the citrate-AgNPs series, together with their associated nanoparticle size distributions, derived using an entropy maximization technique. These data are for the initial citrate-AgNP dispersion before addition of NaCl and early in step three of the titration when 30 mmol L^{-1} NaCl was present. The particle population of diameters between (10 and 18) nm had a significantly larger volume fraction compared to an apparent smaller particle population with diameters ranging from (4 to 6) nm, initially, and (2 to 4) nm at titration step three. Two populations were observed in nearly all data collected across dispersions and titration steps. The principal population was selected when analyzing data for Figure 7a, in order to provide a more direct comparison with the DLS data.

Discussion

General

In assessing the potential hazards to human health and the environment associated with nanoparticles,

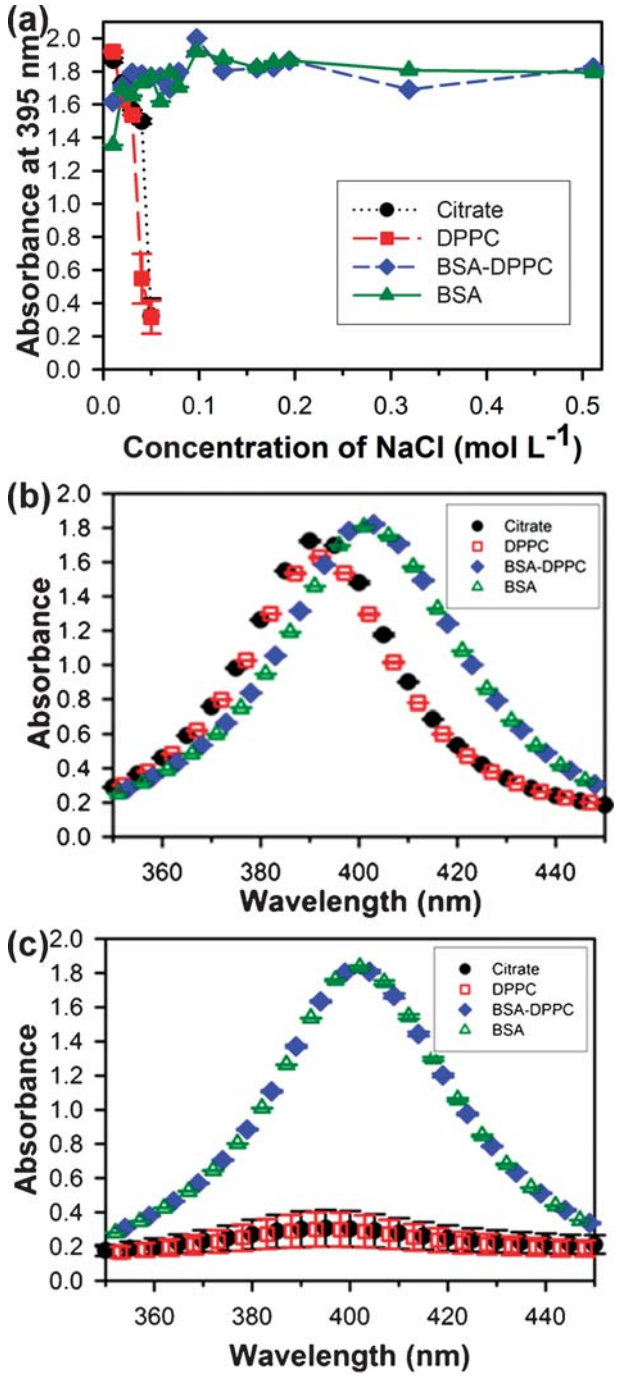

Figure 5. (a) UV-vis absorbance at 395 nm of citrate (black circles), DPPC (red squares), BSA (green triangles), BSA + DPPC (blue diamonds) AgNPs as a function of NaCl concentration. UV-vis spectra are shown for (b) titration step 1 (10 mmol L^{-1}), and (c) titration step 5 (50 mmol L^{-1}), showing the dramatic decrease in absorbance at 395 nm for the citrate and DPPC AgNPs compared to the more stable BSA and BSA + DPPC AgNPs. Uncertainty is one standard deviation from the mean of three measurements; bars are not drawn if uncertainty is smaller than symbol size; lines are to guide eye.

several nano-specific issues arise that impact the design and application of assays and the interpretation of results from these studies. A critical decision that researchers must address when designing experiments, centers around whether an effort should be made to introduce NPs in a well-dispersed single-particle state under relevant conditions, or whether the native (unmodified) state of the NPs should be preserved, regardless of their tendency to aggregate. In other words, is it the native state that should be

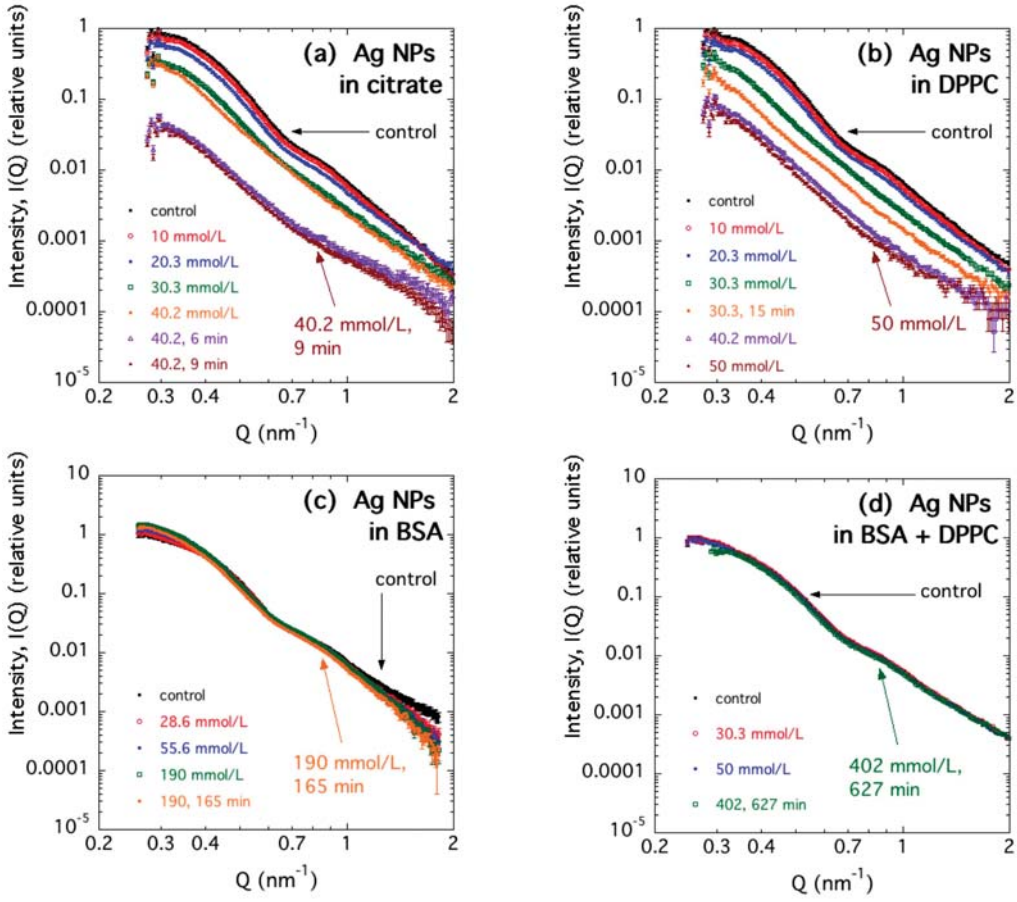

Figure 6. SAXS data associated with typical titration steps in the NaCl titration of (a) citrate-AgNP, (b) DPPC AgNP, (c) BSA AgNP, and (d) BSA + DPPC AgNP dispersions. All intensities are plotted relative to the maximum intensity measured for the initial 'control' condition.

studied, including aggregates, since this represents the reality of the material in a particular environment? This work is not intended to advocate or detract from any possible resolution to this question, even though it is focused on understanding a specific dispersion medium protocol. Rather, it is hoped the results of this study, as they elucidate the effects on stability caused by key constituents in a complex media environment, will enable better design of experiments and interpretation of previously published reports.

One of the key elements of the NIOSH dispersion protocol is the ability to keep engineered NPs dispersed as single primary particles in physiologically relevant conditions (such as high ionic concentrations), purportedly without altering the toxicity profile of the material. As NaCl is the primary constituent of PBS buffer and the most abundant physiological salt, for simplicity only NaCl was used in the titration experiments reported here. Titration with increasing amounts of NaCl allowed estimation of the degree of stabilization against charge screening provided by the BSA, DPPC, or the BSA + DPPC combination. Classical Deryaguin-Landau-Verwey-Overbeek (DLVO) theory (Verwey and Overbeek 1948) shows that colloidal stability is derived from the sum of the van der Waals attractive forces (U_a) and the electrostatic repulsive forces (U_{er}). A third term can be added to reflect steric repulsive interactions (U_{sr}) arising from the bulky nature of the BSA protein coating:

$$U = U_a + U_{er} + U_{sr} \quad (1)$$

The electrostatic repulsive force in Equation (1) is dependent upon the Debye length, κ^{-1} (Chan et al. 2001); further details can be found in the online supplementary information. Because the concentration of electrolyte defines the charge screening length, the approach of titrating NaCl into the AgNP solutions was proposed to elucidate the relative contributions of U_{er} and U_{sr} for each AgNP coating.

The dissolution of AgNPs into Ag^+ was not expected to contribute significantly to the results since all solutions of AgNPs used were purified

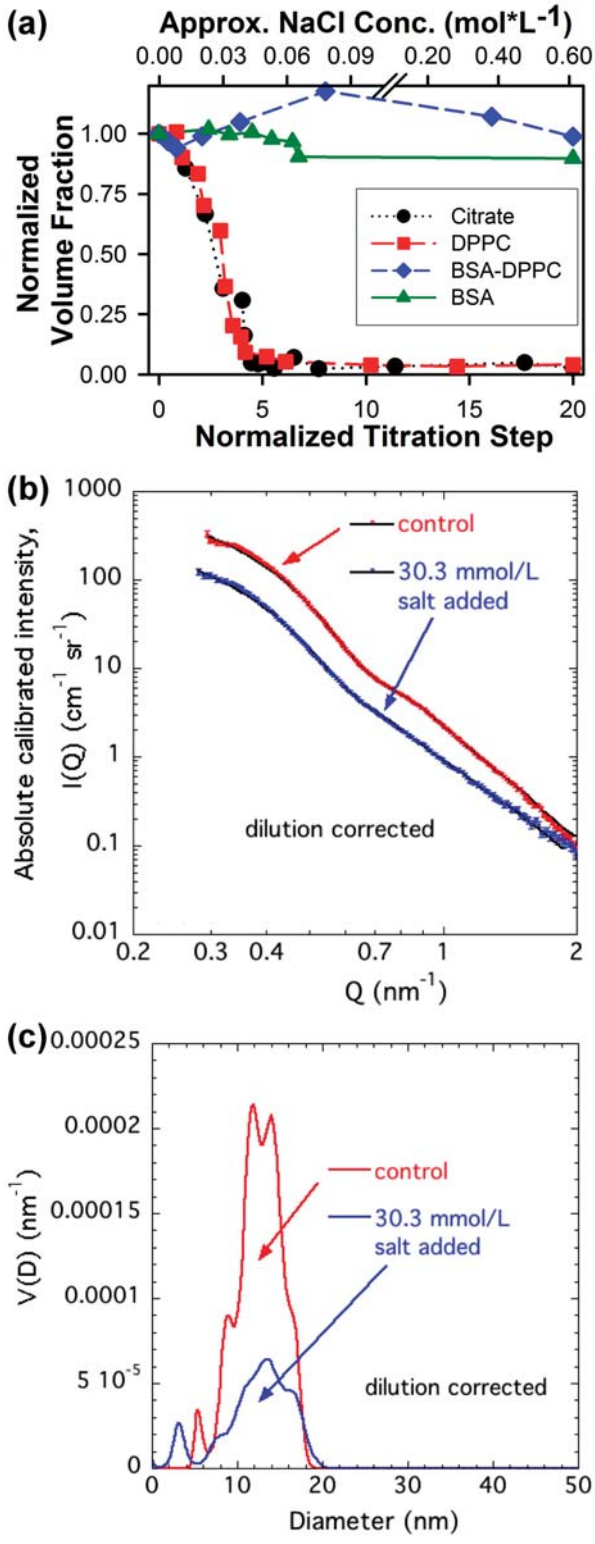

Figure 7. (a) SAXS normalized volume fraction of population with nominal d ≈ 12 nm, during NaCl titration, for citrate (black circles), DPPC (red squares), BSA (green triangles), BSA + DPPC (blue diamonds) AgNPs. Volume fraction is normalized to account for dilution effects from addition of NaCl volumes during the titration. Uncertainty from SAXS data and software routines used is less than the size of the points; lines are to guide eye. (b) Absolute-calibrated SAXS data and (c) entropy-maximized volume fraction nanoparticle size distributions of citrate-AgNPs initially in water (red line) and after titration step three at 30 mmol L^{-1} NaCl (blue line).

immediately after synthesis to remove ions and small molecules, and used within two weeks of synthesis. Furthermore, any Ag^+ that may have been present would be precipitated out of solution by the chloride ions present in the initial aliquot of NaCl.

Changes in hydrodynamic size

The nature of the DLS measurement is such that it can be challenging, though not impossible, to differentiate between homogeneous size increase and agglomeration effects, when conjugation and aggregation phenomena may co-exist (Tsai et al. 2010). A limited increase in the Z_{avg} size could reflect either: (i) An increase in the hydrodynamic envelope due to adsorption of BSA on the AgNP surface, or (ii) formation of small clusters containing very few AgNPs (e.g., dimers, trimers). With the various AgNPs suspended in water initially, there was a 2.2 ± 0.6 nm increase in mean Z_{avg} for BSA + DPPC AgNPs, and a 3.5 ± 0.8 nm increase in diameter for BSA AgNPs, as compared to the native citrate-AgNPs. The mean diameter for BSA in 1X PBS buffer at 6.00 mg mL^{-1} was observed to be 6.9 ± 0.1 nm based on the volume distribution, in agreement with literature values that from (4.1 to 8.2) nm with lower diameters observed at greater protein concentrations (Gun'ko et al. 2003; Ted et al. 2004; Kozak 2005). There was initially sub-monolayer coverage of both types of AgNPs with BSA. Further details of the calculations can be found in the online supplementary information and in Table SI-3.

By comparison to the AgNPs dispersed in deionized water, and considering assumption (i), a single nanoparticle has an average BSA shell thickness that increases with NaCl concentration to a full monolayer. While this would be a significant organic corona, based on the reaction conditions used in this titration, it is theoretically feasible considering that the amount of BSA required to coat every AgNP is less than the number of BSA molecules initially present in solution. Using assumption (ii), it would require 3–5 AgNPs clustered together to fill the effective hydrodynamic volume of the larger structures observed in the BSA AgNP dispersion with ≈ 100 mmol L^{-1} NaCl. Details of these calculations are given in the online supplementary information and Tables SI-4 and SI-5. Above 100 mmol L^{-1} NaCl, there was no further increase in diameter observed beyond the approximately 11 nm increase. For the BSA + DPPC AgNP dispersion, an identical trend to the BSA AgNPs was observed. Combined with the constant PI, the data provide additional evidence that assumption (i) was the correct hypothesis.

As observed by DLS, both the citrate-AgNPs and DPPC AgNPs formed large aggregates from the earliest stages of the titration, while both the BSA AgNP and BSA + DPPC AgNP dispersions exhibited stability throughout the entire range of NaCl concentrations (10 mmol L^{-1} to over 500 mmol L^{-1} NaCl). Because both BSA-containing dispersions of AgNPs followed a stabilized behavior, this suggested the increased colloidal stability at larger salt concentrations is derived primarily from the BSA component as opposed to the DPPC used in the synthetic lung fluid formulation.

The relative constancy of the mean Z_{avg} at NaCl concentrations over 100 mmol L^{-1} for the BSA + DPPC AgNP dispersion compared to the BSA AgNP dispersion suggests that DPPC may exert a subtle effect on the colloidal stability of the AgNPs at higher NaCl concentrations when combined with the BSA. The origin of this effect has not been determined, though one might speculate that DPPC alters the sorption properties of BSA in some way, or perhaps forms a corona around the BSA AgNP core. It is well documented that BSA is an efficient carrier of lipids and fatty acids (roughly 2 fatty acids per BSA), so the DPPC may be associated directly with the BSA and may have some subtle effect on its structure or its interaction with the AgNP surface (Kragh-Hansen 1981). However, to draw conclusions about the exact mechanisms of how DPPC may affect BSA AgNP conjugates would require experimental work that is beyond the scope of the present study.

Confirmation of particle and aggregate structures

In the case of the citrate-AgNPs, the particles were initially well dispersed and provided a high coverage density on the AFM substrate (see Figure 4, top row), even forming multilayers in some regions. As NaCl was added, the AgNPs quickly aggregated out of the solution, as evidenced by the significantly decreased number of single AgNPs and appearance of large aggregate structures. An identical trend was observed for the DPPC AgNPs.

For the BSA-AgNPs, the initial particles appear well-dispersed, but as NaCl was titrated the density of unagglomerated AgNPs adhering to the AFM substrate increased substantially. The increased attachment correlates with the increased sorption of BSA protein on the AgNPs in the presence of NaCl. We speculate that increased BSA surface density on the AgNPs increases affinity of the BSA coated particles for the poly-*L*-lysine coating on the mica substrate. Positively charged poly-*L*-lysine is routinely used by microscopists to attach negatively charged

proteins, such as BSA, to an imaging substrate. The observed height increase of the AgNPs at the higher salt concentrations compared to deionized water provides further evidence that BSA adsorption increases with increasing salt concentration, supporting assumption (i) above.

Moreover, where the DLS revealed a large increase in the Z_{avg} and PI, aggregates of AgNPs were coincidentally observed by AFM. Further, when DLS revealed an increase in Z_{avg} hydrodynamic diameter and no increase in polydispersity (see online Supplementary Figure SI-1), a corresponding small increase in height of the AgNPs was also observed by AFM cross-section analysis with no observation of aggregates.

Of note, images in the left column of Figure 4 represent AgNPs that were deposited from deionized water directly. The AgNPs were observed to have heights that reasonably agreed with the particle diameters derived from DLS and SAXS measurements, as summarized in Supplementary Table SI-6, online. Previous experience with metal nanoparticles suggests that DLS will report slightly larger diameters compared with AFM (NIST 2008b, 2008c, 2008d), as was observed in the series of measurements reported here.

Correlation with changes in particle concentration

The UV-vis absorption data were used to follow the concentration of single AgNPs remaining in solution by reporting the absorbance at or near the SPR peak wavelength. Because large aggregates of AgNPs settle out of solution quickly, and are thus removed from the optical path, the absorbance change at red-shifted wavelengths must be interpreted judiciously. An increased absorbance at red-shifted wavelengths suggests some aggregates were sufficiently stable to remain in solution during the timeframe of the experiment. However, the absence of red-shifted absorbance does not automatically assure the absence of aggregation, only the absence of aggregates in the beam.

The concentration of single AgNPs remaining in solution (reflected by the peak absorbance at 395 nm) decreased rapidly during the first five titration steps for both the citrate-AgNPs and the DPPC AgNPs (Figure 5c). The larger uncertainty in the absorbance values of these dispersions reflects the dynamic process of aggregation occurring on the time scale of the UV-vis observations. For both BSA AgNPs and BSA + DPPC AgNPs, the concentration of single AgNPs in solution remained relatively stable across titration steps, with a low associated uncertainty within each step.

Comparing titration steps two and five, the concentration of single citrate-AgNPs and DPPC AgNPs decreased sharply, although the peak SPR wavelength did not shift appreciably. This suggests massive aggregates formed rapidly in non-BSA dispersions and settled out of the beam. By comparison, the formation of relatively small clusters, containing only a few primary particles, would have been characterized by a red-shifted and broadened peak. While the UV-vis data alone are inconclusive, their interpretation are stronger because they were consistent with DLS data showing aggregates exceeding 1 μm in diameter at 50 mmol L^{-1} NaCl in titration step five; a 1 μm envelope would contain hundreds to thousands of primary particles. It was notable and somewhat surprising that measurable single AgNPs (as manifest by their unshifted SPR absorption peak) appear to remain in suspension despite the rapid formation of large aggregates; clearly, this is an important observation in respect to *in vitro* and *in vivo* testing and the determination of delivered dose. In contrast, the BSA dispersions, to the extent detectable, were likely not forming aggregates with the addition of NaCl, as no broadening or red-shifting of the SPR peak was observed over the course of the experiment; this is entirely consistent with DLS and AFM results discussed previously.

Correlation between DLS, UV-vis and SAXS results

In situ SAXS provides particle core size and size distribution data on polydisperse particle populations complementary to other techniques, as well as volume fraction information that can quantitatively provide particle concentration as a function of the size of the scattering objects.

SAXS titration results for citrate-AgNPs confirmed that the particles were not stabilized against NaCl even at relatively low salt concentrations well below physiological levels. For example, the volume fraction of single citrate-AgNPs in solution, normalized for dilution effects, decreased rapidly during the first five titration steps as shown in Figure 6a. While DLS measurements simply reported a greater uncertainty, SAXS measurements can elucidate the time-dependent changes in the structure and dynamics. When the SAXS data are presented relative to the fractional dwell time (Figure 7a), the concentration of primary particles in the citrate and DPPC AgNP dispersions continued to drop throughout the dwell period after addition of the NaCl solution. These results closely tracked with DLS data in terms of the NaCl concentration at which aggregation begins to be observed, as well as the UV-vis data where the absorbance spectra of the single AgNPs decreases

rapidly during the first five titration steps due to settling of large aggregates.

The DPPC AgNPs exhibited similar behavior to the citrate AgNPs. As further evidenced by other results, the DPPC alone does not provide discernable stabilization. However, the time resolution afforded by synchrotron SAXS experiments, on the order of 10 sec, reveals that, when the accumulated concentration of NaCl was 50 mmol L^{-1}, aggregation was occurring at a rate that revealed time-dependent results throughout the subsequent 12 min of dwell time. The citrate-AgNP dispersions appear to aggregate very quickly (less than 1 min) then reach equilibrium for that step, while the DPPC AgNP dispersions appear to aggregate at a more constant rate. It is important to note that an artifact of this experimental design led to a high but temporary local concentration of NaCl at the point of dispensing, approximately five times higher than the calculated average concentration in the system. Therefore, even at the first titration step of 10 mmol L^{-1}, where citrate-AgNPs are known to be stable on the timescale of minutes, a transient increase to approximately 50 mmol L^{-1} is experienced by approximately 20% of the suspension volume, a concentration where rapid aggregation effects in citrate and DPPC AgNPs have been observed by many techniques. This transient increase rapidly dissipates as the sample is recycled through the reservoir.

It should be noted that the BSA AgNP titration was repeated twice, with different batches of core AgNPs and on different dates; the resulting NP core size distribution was essentially identical for the two experiments. Clearly, the BSA provides significant stabilization to the AgNP dispersion (see Figures 6 and 7).

The step-wise decrease in the intensity of the SAXS curves in Figure 6a and 6b is consistent with the significant UV-vis absorption decrease, and provides further evidence the AgNPs are not stabilized by DPPC alone at the concentration described in the dispersion protocol. Further, the shape of the curves evolves over time in both the citrate-AgNP and DPPC AgNP cases, suggesting that characteristic structural dimensions are changing, something that does not occur with the BSA-stabilized AgNPs. For instance, the knee in the SAXS scattering curve near $Q = 0.9$ nm^{-1} disappeared quite early in the titration, within the first few additions of NaCl, indicating the primary particles were no longer in the beam. The AgNPs did not appear to adhere to the tubing wall or sample reservoir container based on visual inspection after the experiment; however, sediment was observed on the bottom of the sample reservoir in these cases, suggesting that massive aggregation had removed the primary AgNPs from the flow. This was consistent with visual inspection of the UV-vis and DLS cuvettes, which revealed a dark layer of sediment, macroscopic aggregates, upon completion.

From Figures 6c and 6d, it is apparent that the form of the scattering curves was conserved throughout the course of the titration with both BSA AgNPs and BSA + DPCC AgNPs. While the beam was lost temporarily during the latter experiment (and hence fewer data sets are available), the intensity and shape of the SAXS curve was unchanged approximately 18 h after initiating the titration and once the X-ray beam was fully restored. Considering these results with those obtained by UV-vis, DLS and AFM, the structural dimensions and morphology of the scatters are clearly not changing during the long timeframe of this experiment. If the core AgNPs were aggregating into clusters, a distinct change in shape of the SAXS scattering curve would be evident, along with a shift toward lower Q values (as observed in Figure 6a and 6b) for citrate- and DPPC-AgNPs). Since SAXS reveals that the particle cores are remaining singly-dispersed and essentially unchanged in core Ag diameter, this confirms that DLS is in fact reporting an increase in diameter attributable to an expanding organic corona, not an increase in hydrodynamic size due to cluster formation. The difference in diameter between the SAXS data and the DLS data suggests thicker protein coronas than the DLS data alone would suggest, due primarily to the difference in core AgNP size measured between the two techniques (approximately 14 nm for SAXS and 19 nm for DLS).

It is not trivial to point out that the lack of downstream purification may play a role in the effectiveness of this dispersion protocol. Further investigation is required before definitive roles can be assigned, but the data here suggests the ability of AgNPs to adsorb additional BSA from the reservoir of free BSA in the solution phase, and this may play a role in the colloidal stability at high electrolyte concentrations or when the particles are in contact with serum under *in vitro* or *in vivo* conditions. Also of importance will be the ability of the AgNPs to shed their protein corona once they have been phagocytized *in vivo*.

Conclusion

A series of nanoscale silver dispersion conditions were studied under systematic perturbation by complementary *in situ* and *ex situ* techniques in order to interrogate constituent contributions to colloidal stability in a recently reported NIOSH dispersion protocol based on a synthetic lung fluid formulation. SAXS, DLS, UV-vis, and AFM measurements

were collectively considered to provide a much more detailed and robust picture of the dispersion protocol and its impact on AgNP stability behavior than any single technique could provide. BSA is the key ingredient in the NIOSH protocol in terms of providing colloidal stability against high electrolyte concentrations encountered under biological testing conditions (e.g., blood serum, mucus, buffers, cell culture medium, etc.). The phospholipid DPPC, when mixed with BSA, appears to provide slightly better stability at hypertonic salt concentrations than BSA alone, but DPPC did not stabilize effectively by itself. It was determined that BSA increasingly adsorbed onto the surface of the AgNPs as the NaCl concentration increased through the course of a titration. Further investigation is required to determine whether it was the BSA bound to the AgNP surface alone, or perhaps with additional contributions from free BSA in solution, that is largely responsible for observed colloidal stability in the presence of relatively high levels of NaCl. Colloidal stability is a parameter inherently entangled with the surface functionalization of nanoparticles, and since the surface that a nanoparticle presents to a cell is likely to impact its biological fate and toxicity profile, understanding and controlling the nanoparticle surface in dispersion protocols will likely become a key element to correctly interpreting data. The results presented here provide insight into the underlying mechanisms of stability imparted by the NIOSH protocol and its analogs, and gives toxicologists an increased confidence that their studies are introducing well-dispersed core nanoparticles into the animal model or test medium. This work also confirms the broad applicability of the NIOSH approach, since the original formulation was series specific and applied to nanoscale TiO_2 and single-wall carbon nanotubes only; the present study extends the applicability to noble metal nanoparticles.

Acknowledgments

Use of the Advanced Photon Source at Argonne National Laboratory was supported by the U. S. Department of Energy, Office of Science, Office of Basic Energy Sciences, under Contract No. DE-AC02-06CH11357. ChemMatCARS Sector 15 is principally supported by the National Science Foundation/Department of Energy under grant number CHE-0535644. Dr Jan Ilavsky, X-ray Science Division, and Dr Yu-Sheng Chen, ChemMatCARS, both of the Advanced Photon Source, are acknowledged for assistance with measurements and SAXS data reduction. The authors thank Dr John E. Bonevich, NIST Metallurgy Division, for providing the TEM image.

Declaration of interest: The authors report no conflicts of interest. The authors alone are responsible for the content and writing of the paper. *Certain trade names and company products are mentioned in the text or identified in illustrations in order to specify adequately the experimental procedure and equipment used. In no case does such identification imply recommendation or endorsement by National Institute of Standards and Technology, nor does it imply that the products are necessarily the best available for the purpose.

References

Ahamed M, Karns M, Goodson M, Rowe J, Hussain SM, Schlager JJ, Hong YL. 2008. DNA damage response to different surface chemistry of silver nanoparticles in mammalian cells. Toxicol Appl Pharmacol 233:404–410.

Allen AJ, Hackley VA, Jemian PR, Ilavsky J, Raitano JM, Chan SW. 2008. In situ ultra-small-angle X-ray scattering study of the solution-mediated formation and growth of nanocrystalline ceria. J Appl Crystallography 41:918–929.

Aslan K, Lakowicz JR, Geddes CD. 2005. Plasmon light scattering in biology and medicine: New sensing approaches, visions and perspectives. Curr Opin Chem Biol 9:538–544.

Aslan K, Zhang J, Lakowicz JR, Geddes CD. 2004. Saccharide sensing using gold and silver nanoparticles – a review. J Fluorescence 14:391–400.

Astm International. 2009. Inter-laboratory study to establish precision statements for ASTM E2490-09 standard guide for measurement of particle size distribution of nanomaterials in suspension by photon correlation spectroscopy. Research Report E56-1001.

Banerjee IA, Yu LT, MacCuspie RI, Matsui H. 2004. Thiolated peptide nanotube assembly as arrays on patterned Au substrates. Nano Lett 4:2437–2440.

Carey Lea M. 1889. On allotropic forms of silver. Am J Sci 37: 476–491.

Cedervall T, Lynch I, Lindman S, Berggard T, Thulin E, Nilsson H, Dawson KA, Linse S. 2007. Understanding the nanoparticle-protein corona using methods to quantify exchange rates and affinities of proteins for nanoparticles. Proc Natl Acad Sci USA 104:2050–2055.

Chan DYC, Linse P, Petris SN. 2001. Phase separation in deionized colloidal systems: extended Debye-Hückel theory. Langmuir 17:4202–4210.

Cookson DJ, Kirby N, Knott R, Lee M, Schultz D. 2006. Advanced photon source. Strategies for data collection and calibration on the small angle X-ray scattering camera at ChemMatCARS. J Synchrotron Rad 13:440–444.

Duan J, Park K, MacCuspie RI, Vaia RA, Pachter R. 2009. Optical properties of rod-like metallic nanostructures: Insight from theory and experiment. J Phys Chem C 113:15524–15532.

Elghanian R, Storhoff JJ, Mucic RC, Letsinger RL, Mirkin CA. 1997. Selective colorimetric detection of polynucleotides based on the distance-dependent optical properties of gold nanoparticles. Science 277:1078–1081.

Erdely A, Hulderman T, Salmen R, Liston A, Zeidler-Erdely PC, Schwegler-Berry D, Castranova V, Koyama S, Kim YA, Endo M, et al. 2009. Cross-talk between lung and systemic circulation during carbon nanotube respiratory exposure. Potential biomarkers. Nano Lett 9:36–43.

Frederix F, Friedt JM, Choi KH, Laureyn W, Campitelli A, Mondelaers D, Maes G, Borghs G. 2003. Biosensing based on light absorption of nanoscaled gold and silver particles. Analyt Chem 75:6894–6900.

Gao XY, Yu LT, MacCuspie RI, Matsui H. 2005. Controlled growth of Se nanoparticles on Ag nanoparticles in different ratios. Adv Mater 17:426–429.

Gardner GE, Jones MG. 2009. Bacteria buster: Testing antibiotic properties of silver nanoparticles. Am Biol Teach 71:231–234.

Gun'ko VM, Klyueva AV, Levchuk YN, Leboda R. 2003. Photon correlation spectroscopy investigations of proteins. Adv Colloid Interface Sci 105:201–328.

Henig RM. 2007. Our silver-coated future. OnEarth 22–29.

Herzog E, Byrne HJ, Casey A, Davoren M, Lenz AG, Maier KL, Duschl A, Oostingh GJ. 2009a. SWCNT suppress inflammatory mediator responses in human lung epithelium in vitro. Toxicol Appl Pharmacol 234:378–390.

Herzog E, Byrne HJ, Davoren M, Casey A, Duschl A, Oostingh GJ. 2009b. Dispersion medium modulates oxidative stress response of human lung epithelial cells upon exposure to carbon nanomaterial samples. Toxicol Appl Pharmacol 236:276–281.

Hussain SM, Schlager JJ. 2009. Safety evaluation of silver nanoparticles: Inhalation model for chronic exposure. Toxicolog Sci 108:223–224.

Ilavsky J, Jemian PR. 2009. Irena: Tool suite for modeling and analysis of small-angle scattering. J App Cryst 42:347–353.

Jillavenkatesa A, Dapkunas SJ, Lum L-SH. 2001. Particle size characterization – NIST recommended practice guide. Special Publication 960-1.

Kelly KL, Coronado E, Zhao LL, Schatz GC. 2002. The optical properties of metal nanoparticles: The influence of size, shape, and dielectric environment. J Phys Chem B 107:668–677.

Kennedy A, Hackley VA, MacCuspie RI. 2009. NIST-ERDC NanoAg Workshop.

Kim KJ, Sung WS, Suh BK, Moon SK, Choi JS, Kim J, Lee DG. 2009. Antifungal activity and mode of action of silver nano-particles on Candida albicans. Biometals 22:235–242.

Koh AL, Shachaf CM, Elchuri S, Nolan GP, Sinclair R. 2008. Electron microscopy localization and characterization of functionalized composite organic-inorganic SERS nanoparticles on leukemia cells. Ultramicroscopy 109:111–121.

Kozak M. 2005. Glucose isomerase from Streptomyces rubiginosus – potential molecular weight standard for small-angle X-ray scattering. J Appl Crystallogr 38:555–558.

Kragh-Hansen U. 1981. Molecular aspects of ligand binding to serum albumin. Pharmacolog Rev 33:17–53.

Kramer RM, Li C, Carter DC, Stone MO, Naik RR. 2004. Engineered protein cages for nanomaterial synthesis. J Am Chem Soc 126:13282–13286.

Kvitek L, Vanickova M, Panacek A, Soukupova J, Dittrich M, Valentova E, Prucek R, Bancirova M, Milde D, Zboril R. 2009. Initial study on the toxicity of silver nanoparticles (NPs) against Paramecium caudatum. J Phys Chem C 113:4296–4300.

Link S, El-Sayed MA. 1999. Spectral properties and relaxation dynamics of surface plasmon electronic oscillations in gold and silver nanodots and nanorods. J Phys Chem B 103:8410–8426.

Lundqvist M, Stigler J, Elia G, Lynch I, Cedervall T, Dawson KA. 2008. Nanoparticle size and surface properties determine the protein corona with possible implications for biological impacts. Proc Natl Acad Sci USA 105:14265–14270.

Luoma SN. 2008. Silver nanotechnologies and the environment: Old problems or new challenges? PEN 15. The Project on Emerging Nanotechnologies.

Lynch I, Cedervall T, Lundqvist M, Cabaleiro-Lago C, Linse S, Dawson KA. 2007. The nanoparticle-protein complex as a biological entity; a complex fluids and surface science challenge for the 21st century. Adv Colloid Interface Sci 134–135: 167–174.

MacCuspie RI, Banerjee IA, Pejoux C, Gummalla S, Mostowski HS, Krause PR, Matsui H. 2008a. Virus assay using antibody-functionalized peptide nanotubes. Soft Matter 4: 833–839.

MacCuspie RI, Elsen AM, Diamanti SJ, Patton ST, Altfeder I, Jacobs JD, Voevodin AA, Vaia RA. 2010a. Purification-chemical structure-electrical property relationship in gold nanoparticle liquids. Appl Organometallic Chem 24:590–599.

MacCuspie RI. 2010b. Colloidal stability of silver nanoparticles with various surface coatings in biologically relevant conditions. Journal of Nanoparticle Research (submitted).

MacCuspie RI, Nuraje N, Lee SY, Runge A, Matsui H. 2008b. Comparison of electrical properties of viruses studied by AC capacitance scanning probe microscopy. J Am Chem Soc 130:887–891.

Malinsky MD, Kelly KL, Schatz GC, Van Duyne RP. 2001. Chain length dependence and sensing capabilities of the localized surface plasmon resonance of silver nanoparticles chemically modified with alkanethiol self-assembled monolayers. J Am Chem Soc 123:1471–1482.

Matsui H, MacCuspie R. 2001. Metalloporphyrin nanotube fabrication using peptide nanotubes as templates. Nano Lett 1: 671–675.

Maynard A. 2009. Project on emerging nanotechnologies. Woodrow Wilson International Center for Scholars.

Muniz G, Banerjee IA, Yu LT, Djalali R, Matsui H. 2005. Controlled nanocrystal growth on sequence peptide coated nanotubes to fabricate Au, Ag, and Ge nanowires. Abstracts of Papers Am Chem Soc 229:U1154–1154.

Naik RR, Stringer SJ, Agarwal G, Jones SE, Stone MO. 2002. Biomimetic synthesis and patterning of silver nanoparticles. Nature Mater 1:169–172.

Nam KT, Lee YJ, Krauland EM, Kottmann ST, Belcher AM. 2008. Peptide-mediated reduction of silver ions on engineered biological scaffolds. ACS Nano 2: 1480–1486.

National Institute of Standards and Technology (NIST). 2008a. Measuring the size of nanoparticles in aqueous media using batch-mode dynamic light scattering. NIST-NCL Joint Assay Protocol. National Cancer Instititute, Nanotechnology Characterization Laboratory.

National Institute of Standards and Technology (NIST). 2008b. Reference Material 8011, Gold nanoparticles, nominal 10 nm diameter. Gaithersburg, MD: NIST.

National Institute of Standards and Technology (NIST). 2008c. Reference Material 8012, Gold nanoparticles, nominal 30 nm diameter. Gaithersburg, MD: NIST.

National Institute of Standards and Technology (NIST). 2008d. Reference Material 8013, Gold nanoparticles, nominal 60 nm diameter. Gaithersburg, MD: NIST.

Nuraje N, Banerjee IA, MacCuspie RI, Yu LT, Matsui H. 2004. Biological bottom-up assembly of antibody nanotubes on patterned antigen arrays. J Am Chem Soc 126:8088–8089.

Nuraje N, Su K, Samson J, Haboosheh A, MacCuspie RI, Matsui H. 2006. Self-assembly of Au nanoparticle-containing peptide nano-rings on surfaces. Supramolec Chem 18: 429–434.

Perelaer J, Hendriks CE, de Laat AWM, Schubert US. 2009. One-step inkjet printing of conductive silver tracks on polymer substrates. Nanotechnology 20:165303.

Porter D, Sriram K, Wolfarth M, Jefferson A, Schwegler-Berry D, Andrew M, Castranova V. 2008. A biocompatible medium for nanoparticle dispersion. Nanotoxicology 2:144–154.

Potton JA, Daniell GJ, Rainford BD. 1988. Particle size distributions from SANS data using the maximum-entropy method. J App Cryst 21:663–668.

Raffi M, Hussain F, Bhatti TM, Akhter JI, Hameed A, Hasan MM. 2008. Antibacterial characterization of silver nanoparticles against E. coli ATCC-15224. J Mater Sci Technol 24:192–196.

Rahman MF, Wang J, Patterson TA, Saini UT, Robinson BL, Newport GD, Murdock RC, Schlager JJ, Hussain SM, Ali SF. 2009. Expression of genes related to oxidative stress in the mouse brain after exposure to silver-25 nanoparticles. Toxicol Lett 187:15–21.

Sager TM, Castranova V. 2009. Surface area of particle administered versus mass in determining the pulmonary toxicity of ultrafine and fine carbon black: Comparison to ultrafine titanium dioxide. Particle Fibre Toxicol 6:15.

Sager TM, Kommineni C, Castranova V. 2008. Pulmonary response to intratracheal instillation of ultrafine versus fine titanium dioxide: Role of particle surface area. Particle Fibre Toxicol 5:17.

Sager TM, Porter DW, Robinson VA, Lindsley WG, Schwegler-Berry DE, Castranova V. 2007. Improved method to disperse nanoparticles for in vitro and in vivo investigation of toxicity. Nanotoxicology 1:118–129.

Shvedova AA, Kisin ER, Porter D, Schulte P, Kagan VE, Fadeel B, Castranova V. 2009. Mechanisms of pulmonary toxicity and medical applications of carbon nanotubes: Two faces of Janus? Pharmacol Therapeut 121:192–204.

Skebo JE, Grabinski CM, Schrand AM, Schlager JJ, Hussain SM. 2007. Assessment of metal nanoparticle agglomeration, uptake, and interaction using high-illuminating system. Int J Toxicol 26:135–141.

Ted C, Smith KA, Hatton TA. 2004. Photocontrol of protein folding: The interaction of photosensitive surfactants with bovine serum albumin. Biochemistry 44:524–536.

Tien DC, Tseng KH, Liao CY, Huang JC, Tsung TT. 2008. Discovery of ionic silver in silver nanoparticle suspension fabricated by arc discharge method. J Alloys Compounds 463:408–411.

Tomczak MM, Slocik JM, Stone MD, Naik RR. 2007. Bio-based approaches to inorganic material synthesis. Biochem Soc Transact 35:512–515.

Tomczak MM, Slocik JM, Stone MO, Naik RR. 2008. Biofunctionalized nanoparticles and their uses. MRS Bull 33:519–523.

Tsai D-H, DelRio FW, MacCuspie RI, Cho TJ, Zachariah M, Hackley VA. 2010. Competitive adsorption of thiolated polyethylene glycol and mercaptopropionic acid on gold nanoparticles measured by physical characterization methods. Langmuir 26:10325–10333.

Turkevich J, Stevenson PC, Hillier J. 1951. A Study of the nucleation and growth processes in the synthesis of colloidal gold. Discuss Faraday Soc 55.

Verwey EJW, Overbeek JThG. 1948. Theory of the stability of lyophobic colloids. Amsterdam: Elsevier.

Voevodin AA, Vaia RA, Patton ST, Diamanti S, Pender M, Yoonessi M, Brubaker J, Hu JJ, Sanders JH, Phillips BS, et al. 2007. Nanoparticle-wetted surfaces for relays and energy transmission contacts. Small 3:1957–1963.

Wiesner MR, Lowry GV, Jones KL, Hochella J, Di Giulio RT, Casman E, Bernhardt ES. 2009. Decreasing uncertainties in assessing environmental exposure, risk, and ecological implications of nanomaterials. Environ Sci Technol 43:6458–6462.

Wijnhoven SWP, Peijnenburg WJGM, Herberts CA, Hagens WI, Oomen AG, Heugens EHW, Roszek B, Bisschops J, Gosens I, Van De Meent D, et al. 2009. Nano-silver – a review of available data and knowledge gaps in human and environmental risk assessment. Nanotoxicology 3:109–138.

Yeo MK, Yoon JW. 2009. Comparison of the effects of nano-silver antibacterial coatings and silver ions on zebrafish embryogenesis. Molec Cellular Toxicol 5:23–31.

Yu LT, Banerjee IA, Matsui H. 2003. Direct growth of shape-controlled nanocrystals on nanotubes via biological recognition. J Am Chem Soc 125:14837–14840.

Supplementary material available online

Supporting information including SAXS NaCl titration details, extended calculations, and extended details of observed measurements are available online.